



HAL
open science

Structured deformation of damaged continua with cohesive-frictional sliding rough fractures

Marc Louis Maurice François, Gianni Royer-Carfagni

► **To cite this version:**

Marc Louis Maurice François, Gianni Royer-Carfagni. Structured deformation of damaged continua with cohesive-frictional sliding rough fractures. *European Journal of Mechanics - A/Solids*, 2005, 24, pp.644-660. 10.1016/j.euromechsol.2004.12.005 . hal-00984322

HAL Id: hal-00984322

<https://hal.science/hal-00984322>

Submitted on 31 Jul 2023

HAL is a multi-disciplinary open access archive for the deposit and dissemination of scientific research documents, whether they are published or not. The documents may come from teaching and research institutions in France or abroad, or from public or private research centers.

L'archive ouverte pluridisciplinaire **HAL**, est destinée au dépôt et à la diffusion de documents scientifiques de niveau recherche, publiés ou non, émanant des établissements d'enseignement et de recherche français ou étrangers, des laboratoires publics ou privés.

Structured deformation of damaged continua with cohesive-frictional sliding rough fractures

Marc François^{a,*}, Gianni Royer-Carfagni^b

^a *Department of Civil Engineering and Environment, LMT Cachan, 61, avenue du President Wilson, 94235 Cachan cedex, France*

^b *Dipartimento di Ingegneria Civile, dell'Ambiente, del Territorio e Architettura, Università di Parma, Parco area delle Scienze 181/A, I43100 Parma, Italy*

Abstract

The influence of cohesive-frictional crack sliding on the response of quasi-brittle fractured bodies and, in particular, the shear-induced dilatation due to crack surmounting, are here considered by assuming an equivalent shape function for crack-lip roughness. The deformation is modeled at the continuum level *via* structured deformation theory, introducing relevant kinematical descriptors that are now set in the classical thermodynamic formulation for generalized standard materials. The resulting model lies in the “simplified model” class, since internal variables may be reduced to one scalar parameter associated with the smeared-crack slip. Remarkably, even in the presence of friction, the structured-deformation approach renders the model fully-associated in type, a property particularly relevant for F.E. implementation. In the simplest case no evolution of crack density and orientation is supposed, and despite this simplification, a good description of the response of cracked masonry or concrete walls under seismic-like shear are provided by the model, whose calibration is obtainable through *ad hoc* tests. Interesting instabilities in the shearing path are exhibited, suggesting as well a possible generalization of the Mohr–Coulomb criterion.

Keywords: Damage mechanics; Structured deformations; Rough cracks; Friction; Cohesion; Crack sliding; Quasi-brittle materials; Concrete; Masonry; Geomaterials

1. Introduction

Due to the effect of cohesive forces opposing fracture opening, a diffuse micro-crack framework – rather than a dominant main crack – is developed under load in materials like concrete, ceramics, geomaterials or masonry, hence the name “quasi-brittle” (Bazant and Planas, 1998) by which such materials are usually referred to. Substantial progress in the description of this degradation process has been made during the last 20 years (Jefferson, 2003) using damage mechanics theory (Lemaitre and Chaboche, 1984), which presents some advantages with respect to classical fracture mechanics.

Damage mechanics historically begun with pure “macro” approaches, in which some scalar parameter was used to describe the fall of elastic properties due to microcrack evolution (Kachanov, 1986). The main idea of the successive micro–macro

* Corresponding author.

E-mail addresses: francois@lmt.ens-cachan.fr (M. François), gianni.royer@unipr.it (G. Royer-Carfagni).

approach consisted in homogenizing some local fracture mechanics solutions at the representative volume element (RVE) scale. The actual crack distribution, affecting the macro-response (Kaufmann and Marty, 1998; Belletti, Cerioni and Iori, 2001), could be determined from the macro-stress or -strain state (Steigman, 1991; Mazars, 1986; Ragueneau, La Borderie and Mazars, 2000), or could be supposed established by the first overcoming tensile stress in the virgin material (Pang and Hsu, 1996). The homogenization may (or may not) take into account interference between cracks (Benveniste, Dvorak and Wung, 1989; Fond, Fléjou and Berthaud, 1995) in case of high crack density, while the evolution laws can (or cannot) suppose fixed or not the crack orientation, considering as internal variables crack opening and crack sliding in the irreversible process thermodynamic approach (Andrieux, Bamberger and Marigo, 1986; Halm and Dragon, 1996, 1998; Pensée and Kondo, 2001). Possible cohesive forces (due to fiber bridging or grain bridging, aggregate frictional interlock, crack overlap etc.) can as well be taken into account in the Barenblatt (1962) sense.

The above class of models usually assume that cracks are flat or penny shaped (Onat, 1984). Nevertheless, it is well known that in quasi-brittle materials cracks exhibit considerable roughness, usually due to small-size heterogeneities (such as sand or stone aggregates in concrete). What is more, the measured roughness presents well-known self-similarity properties (Maji and Wang, 1992; Schmittbuhl, Roux and Berthaud, 1994; Amitrano and Schmittbuhl, 2002), emphasizing once more that roughness should not be neglected in any damage model for quasi-brittle materials. Indeed, at the macro level many classical tests, such as the shearing of wall panels, exhibit shear-induced dilatations that are due to rough-crack opening due to lip-sliding. In the fracture mechanics field, relevant models (Patton, 1996; Dyskin and Galybin, 2001) have been proposed to reproduce this effect but, to our knowledge, no micro–macro damage model takes into account roughness at the micro-level in a consistent thermodynamic approach.

In general, the continuum description is not trouble-free. As a rule, the cohesive forces bridging the crack surfaces gradually diminish the wider the crack opening is, so that the resulting equivalent continuum exhibit a strain softening response, which may lead to some theoretical difficulties such as strain localization. A consistent way to perform the limit of discontinuous deformations, as the average distance between opening/sliding cracks goes to zero, is furnished by structured deformation theory, recently advanced by Del Piero and Owen (1993, 2000) in order to develop earlier ideas in a rigorous mathematical framework. Roughly speaking, a structured deformation is the combination of a classical “regular” deformation with a “singular” deformation, produced by micro-disarrangements. This distinction is important in view of a thermodynamically-motivated theory because crack sliding, and the consequent induced crack-opening, lead to plasticity-like deformation splitting, while preserving their original mechanical significance.

The model here proposed, albeit tentatively, represents a first attempt at respond to the demand of a damage model involving rough fractures. The proposed approach is based upon structured deformation theory and it is built within the irreversible process framework, following the generalized standard-material theory (Halphen and Nguyen, 1975). The model structure, besides assuring easy numerical implementation, allows a straightforward extension to contemplate other approaches in the field of damage models. For example, in this introductory paper the crack pattern is supposed to be assigned and invariable during the loading process, but an evolution law for cracks could be easily added without major modifications, and it will be done in further work.

The plan of the paper is as follows. Relying upon structured deformation theory, a simple mesoscopic model for cracked materials is presented in Section 2, motivated by micromechanical considerations on rough crack sliding. In Section 3, the structured-deformation description is interpreted in a thermodynamic framework for irreversible processes by considering crack sliding as an internal variable associated with a proper thermodynamic force, through which macroscopic dissipation and yield criteria are deduced. In Section 4 the theory is applied to cracked materials under shear and confinement, showing a surprisingly wide range of material instabilities. Finally, a possible way to calibrate the model according to the experimental evidence is discussed in the concluding section.

2. Micromechanics via structured deformation theory

For the sake of simplicity, this study will treat a two-dimensional case only. Consider a membrane element made of a quasi-brittle material in generalized plane stress, completely damaged by diffuse micro-cracks. Suppose that in any region \mathfrak{R} , whose diameter is much larger than the panel thickness and crack spacing, but much smaller than the panel size, the orientation, spacing and characteristic length of the micro-cracks is uniform. Fig. 2.1(a) represents, for example, a damaged concrete panel with the aforementioned properties. We surmise that under moderate loading neither new cracks are nucleated nor crack length varies, although crack gliding is allowed. The punctual stress and strain will be very complicated, but an average view of such complex phenomena can be obtained by considering an *equivalent* crack layout for the panel, where cracks are parallel, equidistant and with the same profile. A representative volume element RVE for such an *ideal* material is drawn in Fig. 2.1(b). The orthogonal base $\{\mathbf{e}_1, \mathbf{e}_2\}$, used in the following, has been chosen such that \mathbf{e}_1 is at right angle to the crack average plane.

Let $\omega: \mathbb{R} \rightarrow \mathbb{R}$ represent a continuously differentiable, symmetric, even, periodic function, with mathematical period p . With respect to a (ξ, η) reference system, with ξ and η parallel to \mathbf{e}_2 and \mathbf{e}_1 respectively, the crack-lip shape is identified by

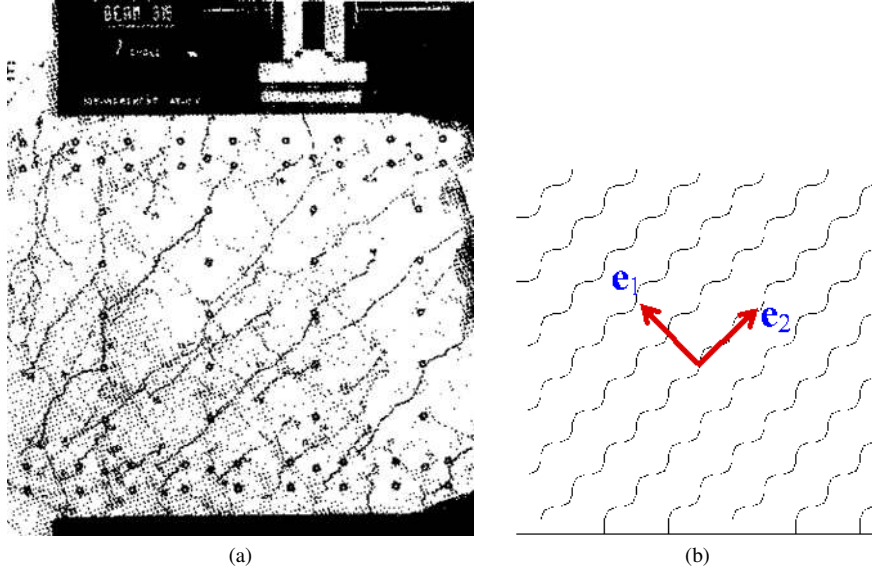


Fig. 2.1. (a) Photograph of a representative volume element of a cracked membrane. (b) Equivalent model with parallel and equidistant through-cracks.

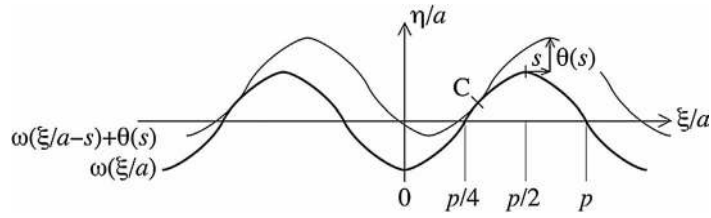


Fig. 2.2. The crack wave function ω and the translation-induced shear dilatation.

the graph of $\eta = a\omega(\xi/a)$, represented with a bold face line in Fig. 2.2. Here a is a reference length, so that crack wave-length results equal to pa .

Assume that the crack shape is symmetric, i.e., it can be made to coincide with itself after the combination of a reflection in its average line and a translation of half the wave-length, so that

$$\omega(p/4 + \xi/a) = -\omega(p/4 - \xi/a), \quad \forall \xi. \quad (2.1)$$

If the upper lip glides with respect to the lower as in Fig. 2.2, mode II shearing clearly induces mode I opening due to surmounting. The main hypothesis here introduced is that the lips, at first fitting together, maintain at least a contact point while sliding, so that their relative translation uniquely determines the crack opening. For convenience, we will denote with $s \cdot a$ and with $a\theta(s)$ the shearing and the corresponding opening, where s is a non-dimensional parameter and $\theta(\cdot)$ will be referred to as the *separation function*. Keeping the reference axes anchored to the lower crack lip as in Fig. 2.2, after the sliding s the equation of the upper crack lip results $\eta = a\omega(\xi/a - s) + a\theta(s)$. If $C \equiv (\xi_c, a\omega(\xi_c/a)) \equiv (\xi_c, a\omega(\xi_c/a - s) + a\theta(s))$ denotes the contact point, due to the aforementioned symmetry (2.1), provided the function $\omega(\xi_c/a)$ is convex on $[-p/4, p/4]$, one finds:

$$\begin{aligned} \xi_c/a &= s/2 + p/4 + kp, & \text{if } s \in]0, p/2] + kp, \quad k \in \mathbb{Z}, \\ \xi_c/a &= s/2 - p/4 + kp, & \text{if } s \in]-p/2, 0] + kp, \quad k \in \mathbb{Z}. \end{aligned} \quad (2.2)$$

Then $\theta(s)$, taking into account that ω is even and (2.1), reads:

$$\begin{aligned} \theta(s) &= \omega(p/4 + s/2) - \omega(p/4 - s/2) = 2\omega(p/4 + s/2), & \text{if } s \in]0, p/2] + kp, \\ \theta(s) &= \omega(p/4 - s/2) - \omega(p/4 + s/2) = -2\omega(p/4 + s/2), & \text{if } s \in]-p/2, 0] + kp. \end{aligned} \quad (2.3)$$

to the distortion of the material still integer. Del Piero and Owen (2000) call the pairing (\mathbf{g}, \mathbf{G}) a *structured deformation* and constructed a rigorous mathematical framework for the relevant theory.

Formula (2.8) implicitly assumes that the displacement field varies smoothly throughout the panel, so that in any region whose size is comparable with those of the RVE the *macroscopic* strain is homogeneous and the rotation uniform. Assuming that the gradients of $u(x, y)$ and $v(x, y)$, as well as $s(x, y)$ and $\theta(s(x, y))$ are quantities small of the first order, the Green's strain $(\mathbf{G}^T \mathbf{G} - \mathbf{I})/2$, due to the elasticity of the material, may be approximated by the *elastic infinitesimal strain*

$$\boldsymbol{\varepsilon}^e(x, y) = \frac{1}{2}(\nabla \mathbf{g} + \nabla \mathbf{g}^T) - \mathbf{I} - \frac{1}{2}(\mathbf{M} + \mathbf{M}^T) = \boldsymbol{\varepsilon}(x, y) - \theta(s(x, y))\mathbf{E}_{11}(x, y) - s(x, y)\mathbf{E}_{12}(x, y), \quad (2.9)$$

where

$$\boldsymbol{\varepsilon}(x, y) = \begin{bmatrix} u_{,x} & (u_{,y} + v_{,x})/2 \\ (u_{,y} + v_{,x})/2 & v_{,y} \end{bmatrix} \quad (2.10)$$

represents the *macroscopic infinitesimal strain*, and

$$\mathbf{E}_{11}(x, y) = \mathbf{e}_1(x, y) \otimes \mathbf{e}_1(x, y), \quad \mathbf{E}_{12}(x, y) = \frac{\mathbf{e}_1(x, y) \otimes \mathbf{e}_2(x, y) + \mathbf{e}_2(x, y) \otimes \mathbf{e}_1(x, y)}{2}. \quad (2.11)$$

The quantity

$$\boldsymbol{\varepsilon}^s(x, y) = \theta(s(x, y))\mathbf{E}_{11}(x, y) + s(x, y)\mathbf{E}_{12}(x, y) \quad (2.12)$$

represents instead the (infinitesimal) singular part of the strain, i.e. that due to the microscopic disarrangements. The macroscopic strain $\boldsymbol{\varepsilon}$ is obtained with respect to the hypothesis of its partition in the elastic part $\boldsymbol{\varepsilon}^e$ (due to the elasticity of the undamaged *lamellae* in between the cracks) and the structured deformation part $\boldsymbol{\varepsilon}^s$ due to the disarrangements, leading to the plastic-like deformation splitting

$$\boldsymbol{\varepsilon} = \boldsymbol{\varepsilon}^e + \boldsymbol{\varepsilon}^s. \quad (2.13)$$

Of course, this theory can account neither for the local stress fields consequent to Hertzian contact, nor for crack profile modifications due to surface wear. Consequently, as will be discussed in the concluding Section, the present model can only apply to moderately-loaded damaged materials.

Compatibility conditions must be added to assure that the complete strain field $\boldsymbol{\varepsilon}$ derives from a displacement field (u, v) and from a field of disarrangements which do not interfere with one another. These give rise to mathematical conditions that the scalar fields $\theta(x, y)$ and $s(x, y)$ and the tensor fields $\mathbf{E}_{11}(x, y)$ and $\mathbf{E}_{12}(x, y)$ have to satisfy to be solutions of any boundary value problem. In this paper, however, we shall remain at the RVE scale, i.e. it will be supposed that fractures are straight and parallel and that boundary conditions, displacement field and disarrangements are all homogeneous in the body. Consequently, there will be no need to deal with the problem of the compatibility of deformation, which will become indeed of crucial importance in the general case.

In any case, it should be emphasized that structured deformation theory allows to describe highly discontinuous displacements using continuous fields, introducing kinematical descriptors, such as the shear s and the separation function $\theta(s)$, that allow to recognize which part of the macroscopic deformation is indeed due to microstructural disarrangements. This represents not only a simplified notation, but could have been as well the starting point of the study since, as discussed in the concluding section, in general it is easier to experimentally measure the average separation function $\theta(s)$ with respect to the average shear s rather than identify the microscopic complexity of crack slinding and opening. This ‘‘macro’’ point of view allows to forget about the length-scale a , despite here the equivalent crack-model has been introduced to furnish a micro-mechanical motivation to the model. An ad hoc experimental study by *post-mortem* point-by-point measurement of the fracture profile (Schmittbuhl, Roux and Berthaud, 1994) will be considered in the future in order to directly determine $\omega(s)$. Another possibility is offered by an indirect estimate of $\omega(s)$ through the assessment of $\theta(s)$, using for example an experimental apparatus of the type proposed by Walraven and Reinhardt (1981), as mentioned in section five.

3. Thermodynamical framework

The present section details the thermodynamic framework for a damaged material where, within a classical formulation (Halphen and Nguyen, 1975), one of the internal state variables is given by the crack slide s . At constant temperature, the model is defined through the Helmholtz's free energy per unit mass ψ and the yield function f , correlating the thermodynamic force S associated with s .

3.1. Helmholtz free energy

The state variables suggested by the micro-mechanics are the total strain $\boldsymbol{\varepsilon}$ of (2.13) and the slip s , which defines the structured part of the deformation $\boldsymbol{\varepsilon}^s$ as per (2.12). In particular, recall that the tensors $\mathbf{E}_{11}(x, y)$ and $\mathbf{E}_{12}(x, y)$, defined in (2.11), as well as the function $\theta(s)$ of (2.3), are determined by the initial microcrack configuration for the damaged material and, since this is supposed to be invariable during the loading process, such quantities are retained as problem *data*.

Considering isothermal evolution, the Helmholtz free energy is defined as the reversible elastic energy. Let \mathbb{C} represent the fourth order elasticity tensor for the undamaged (uncracked) material, supposed linear elastic. Since elastic energy is stored in the integer material portions in between the microcracks, using the expression (2.9) for the elastic component of the strain $\boldsymbol{\varepsilon}^e$ the free energy *per* unit mass reads²

$$\Psi[\boldsymbol{\varepsilon}, s] = \frac{1}{2\rho}(\boldsymbol{\varepsilon} - \theta(s)\mathbf{E}_{11} - s\mathbf{E}_{12}) \cdot \mathbb{C}[\boldsymbol{\varepsilon} - \theta(s)\mathbf{E}_{11} - s\mathbf{E}_{12}], \quad (3.1)$$

where ρ is the material density. When the material matrix is isotropic, it is convenient to split each tensor into hydrostatic and deviatoric (traceless) parts, denoted with the apex ‘‘H’’ and ‘‘D’’, respectively. Recall that \mathbf{E}_{11} and \mathbf{E}_{12} are orthogonal, i.e. $\mathbf{E}_{11} \cdot \mathbf{E}_{12} = 0$, and that \mathbf{E}_{12} is deviatoric, i.e. $\mathbf{E}_{12}^D = \mathbf{E}_{12}$ and $\mathbf{E}_{12}^H = 0$. Then, the previous equation can be re-written in a simpler form with respect to the shear modulus μ and the compression modulus K as follows:

$$2\rho\Psi[\boldsymbol{\varepsilon}, s] = 2\mu[\boldsymbol{\varepsilon}^D - \theta(s)\mathbf{E}_{11}^D - s\mathbf{E}_{12}]^2 + 3K[\boldsymbol{\varepsilon}^H - \theta(s)\mathbf{E}_{11}^H]^2. \quad (3.2)$$

Here, $3K$ and 2μ are the Kelvin’s moduli, while $\mathbf{E}_{11}^D, \mathbf{E}_{11}^H$ are the deviatoric and hydrostatic part of \mathbf{E}_{11} , respectively.

3.2. Associated thermodynamic forces

Similarly, the stress $\boldsymbol{\sigma}$ is split into the deviatoric and hydrostatic parts $\boldsymbol{\sigma}^D$ and $\boldsymbol{\sigma}^H$. For an isotropic material, these correspond to the thermodynamic forces associated with the deviatoric $\boldsymbol{\varepsilon}^D$ and hydrostatic $\boldsymbol{\varepsilon}^H$ parts of the *macroscopic* strain respectively, and are obtained by derivation of the free energy with respect to $\boldsymbol{\varepsilon}^D$ and $\boldsymbol{\varepsilon}^H$, i.e.

$$\boldsymbol{\sigma}^D = 2\mu[\boldsymbol{\varepsilon}^D - \theta(s)\mathbf{E}_{11}^D - s\mathbf{E}_{12}], \quad \boldsymbol{\sigma}^H = 3K[\boldsymbol{\varepsilon}^H - \theta(s)\mathbf{E}_{11}^H]. \quad (3.3)$$

When $s = 0$, from (2.3) also $\theta(s) = 0$ and isotropic elasticity is recovered. Again from (2.3), setting $s = kp$, $k \in \mathbb{Z}$, leads to $\theta(kp) = 0$, which shows that a p -periodic crack shift does not affect the hydrostatic part of the elasticity law. We observe, in passing, that an alternative point of view may consist in regarding $\boldsymbol{\varepsilon}^s = \theta(s)\mathbf{E}_{11} + s\mathbf{E}_{12}$ to be equivalent to a plastic strain since, as in classical plasticity theory, from (3.1) the stress is given by $\mathbb{C}(\boldsymbol{\varepsilon} - \boldsymbol{\varepsilon}^s)$. However, the similarity stops here as the evolution law presented in the forthcoming part will be different.

Following the standard generalized material framework (Halphen and Nguyen, 1975), the thermodynamic force S associated with s is the partial derivative of the Helmholtz free energy per unit volume with respect to s , i.e. $S = -\partial(\rho\Psi)/\partial s$ (the minus sign is due to a thermodynamical convention). For the case at hand, it is clear that S , coinciding with the decrease in elastic energy per unitary variation of s , represents the driving force for crack slip. In case of isotropic materials, from (3.2) we obtain

$$S = 2\mu[(\theta'\mathbf{E}_{11}^D + \mathbf{E}_{12}) \cdot \boldsymbol{\varepsilon}^D - \mathbf{E}_{11}^D \cdot \mathbf{E}_{11}^D \theta\theta' - \mathbf{E}_{12} \cdot \mathbf{E}_{12}s] + 3K\theta'[\mathbf{E}_{11}^H \cdot \boldsymbol{\varepsilon}^H - \mathbf{E}_{11}^H \cdot \mathbf{E}_{11}^H \theta], \quad (3.4)$$

where θ' denotes the derivative of θ and $\varepsilon_{11}, \varepsilon_{12}, \varepsilon_{22}$ are the strain components referred to the orthogonal base $\{\mathbf{e}_1, \mathbf{e}_2\}$, being \mathbf{e}_1 orthogonal to crack average plane. Using the constitutive relations (2.12) (2.13) and (3.3), expression (3.4) can be significantly rewritten in terms of the stress $\boldsymbol{\sigma}$ in the form

$$S = \boldsymbol{\sigma} \cdot (\theta'\mathbf{E}_{11} + \mathbf{E}_{12}), \quad (3.5)$$

is obtained. Here, $\boldsymbol{\sigma} \cdot \mathbf{E}_{12}$ is the shear stress acting at the crack level while $\boldsymbol{\sigma} \cdot \mathbf{E}_{11}$, with \mathbf{E}_{11} as in (2.11)₁, coincides with $\mathbf{e}_1 \cdot \boldsymbol{\sigma} \mathbf{e}_1$ and represents the normal component of stress. Thus, we infer from (3.5) that not only is the driving force S produced by the shear $\boldsymbol{\sigma} \cdot \mathbf{E}_{12}$, but a significant role is also played by the term $\theta'\boldsymbol{\sigma} \cdot \mathbf{E}_{11}$, which represents the ‘‘dilation-induced-shear’’.

3.3. Convex of elasticity

It is natural to define the elastic region (here referred to as ‘‘convex’’ of elasticity) with respect to the associated thermodynamic forces $(\boldsymbol{\sigma}, S)$. For example, in order to retain a Coulomb-like response we may introduce the function

$$f(\boldsymbol{\sigma}, S) = |S| - (B - \varphi\boldsymbol{\sigma} \cdot \mathbf{E}_{11}), \quad (3.6)$$

² In the following we will denote with ‘‘ \cdot ’’ the inner product between vectors and tensors, i.e. $\mathbf{w} \cdot \mathbf{v} = v_i w_i$, $\mathbf{A} \cdot \mathbf{B} = A_{ij} B_{ij}$, where repeated indices signifies summation. The notation is rather standard.

which defines the elasticity domain through condition $f(\boldsymbol{\sigma}, S) < 0$. Here, φ is the frictional coefficient and the constant B represents a cohesive contribution, relative to observed crack-bridging in quasi-brittle materials (Maji and Wang, 1992) and consistent with Barenblatt's approach (Barenblatt, 1962).

Notice that $\boldsymbol{\sigma} \cdot \mathbf{E}_{11} < 0$ specifies that the crack is "in the average" compressed (recall that $\boldsymbol{\sigma}$ is a macroscopic stress defined at a material scale much larger than the crack roughness), so that the borderline case when $B = 0$ corresponds to unilateral Coulomb's frictional law. In fact we notice from (3.6) that when $B = 0$ condition $\boldsymbol{\sigma} \cdot \mathbf{E}_{11} > 0$ is not admissible, since the body would split into pieces when pulled across the crack plane. Besides, the compressive normal stress $\boldsymbol{\sigma} \cdot \mathbf{E}_{11} < 0$, weighted by φ , increases the size of the elastic domain. More precisely, we should mention that the presented formulation is not the exact Coulomb's law, which should act according the tangent plane at the contact point C (Fig. 2.2), but an "average" frictional law, effective at the level of average crack plane. The second borderline case, when $\varphi = 0$, corresponds to cohesive sliding: in fact, we have from (3.6) that $|S|$ remains constants at yielding, independently of the compressive stress.

The combinations of these two cases furnishes the admissibility condition

$$\boldsymbol{\sigma} \cdot \mathbf{E}_{11} < B/\varphi. \quad (3.7)$$

In words, the simultaneous presence of cohesion and friction allows to withstand also moderate tensile stress at right angle to the crack plane.

3.4. Flow rule

At yielding ($f = 0$), the evolution for the state variable s is determined from the consistency equation $df = 0$ and generalized normality rule (Halphen and Nguyen, 1975), saying that

$$\dot{s} = \frac{\partial f}{\partial S} \dot{\lambda} = \text{sgn}(S) \dot{\lambda}, \quad (3.8)$$

where λ is analogous to the classic plastic multiplier with $\dot{\lambda} > 0$. In this respect, the model can be considered associated, i.e. the dissipation pseudo-potential coincides with the yield function. In particular, since from (3.8) \dot{s} has the same sign of S , it follows that the yield condition deriving from (3.6) can be written in the form,

$$\begin{cases} S = B - \varphi \boldsymbol{\sigma} \cdot \mathbf{E}_{11} & \text{if } \dot{s} > 0, \\ S = -(B - \varphi \boldsymbol{\sigma} \cdot \mathbf{E}_{11}) & \text{if } \dot{s} < 0, \\ |S| \leq B - \varphi \boldsymbol{\sigma} \cdot \mathbf{E}_{11} & \text{if } \dot{s} = 0, \end{cases} \quad (3.9)$$

where $B - \varphi \boldsymbol{\sigma} \cdot \mathbf{E}_{11}$ is positive. This is a further indication that S is correlated with the effective shearing force in the average crack plane.

3.5. Positiveness of the dissipation

The second principle of thermodynamics states that the intrinsic dissipation \dot{D} must be positive. From the general theory (Lemaitre, 1992), \dot{D} equals the sum of the products $A_k \dot{V}_k$, where A_k denotes the thermodynamic force associated with the internal state variable V_k . For the case at hand, $A_k \equiv S$ and $\dot{V}_k \equiv \dot{s}$ and, from (3.8), we can notice that the second principle is naturally fulfilled, i.e. $\dot{D} = S \dot{s} > 0$.

Moreover, from (3.9), the intrinsic dissipation \dot{D} takes the simple form

$$\dot{D} = (B - \varphi \boldsymbol{\sigma} \cdot \mathbf{E}_{11}) |\dot{s}|, \quad (3.10)$$

from which we find again that the admissibility condition (3.7), i.e. $\boldsymbol{\sigma} \cdot \mathbf{E}_{11} < B/\varphi$, is strictly correlated to the positiveness of the dissipation.

4. Response under shear and tension-compression

The response of a RVE under shear and simultaneously loaded at right angle to the crack average plane is now examined in detail.

4.1. General considerations

Assume that the stress state is homogeneous and of the form $\boldsymbol{\sigma} = \sigma \mathbf{e}_1 \otimes \mathbf{e}_1 + \tau (\mathbf{e}_1 \otimes \mathbf{e}_2 + \mathbf{e}_2 \otimes \mathbf{e}_1)$ where, as in Fig. 2.1, \mathbf{e}_1 and \mathbf{e}_2 are orthogonal and parallel to the crack average plane respectively. From (3.5), the thermodynamical variable S associated with the slip s is

$$S = \sigma \theta'(s) + \tau. \quad (4.1)$$

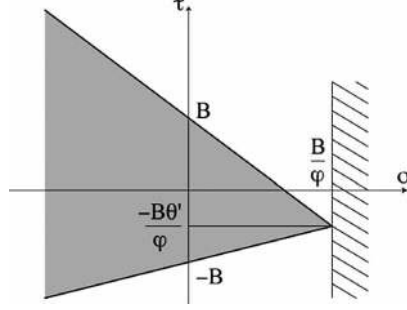


Fig. 4.1. The elastic domain for a given state $(s, \theta'(s))$.

In words, S is the sum of the imposed shearing τ and of the term $\sigma\theta'$, which has a precise mechanical interpretation. Recall that crack lips are supposed to remain in contact during a relative translation and, looking at Fig. 2.2, it is clear that pulling the specimens may cause crack sliding. At each instant, the relative velocity of the gliding contact points is parallel to the common tangent plane to the crack lip profiles, which forms an angle θ' with respect to the crack average plane, so that one can interpret $\sigma\theta'$ as the shear induced by the stress σ , acting at right angle to the crack average plane. The equivalence is also evident in terms of energy since the dissipation reads

$$\dot{D} = S\dot{s} = \sigma\dot{\theta} + \tau\dot{s}, \quad (4.2)$$

where $\tau\dot{s}$ is the power dissipated by the shear stress and $\sigma\dot{\theta}$ the power dissipated by the tensile stress in the extension that accompanies crack sliding. From (3.6) and (4.1), the elastic domain at a given state s is defined by the inequality

$$|\sigma\theta'(s) + \tau| \leq B - \varphi\sigma, \quad (4.3)$$

where $B - \varphi\sigma > 0$ from the admissibility conditions of Section 3.3. This equation is analogous to some relevant conditions usually employed in rough-crack fracture mechanics (Patton, 1996; Dyskin and Galybin, 2001), although here it has been derived in a different way.

In the (σ, τ) plane, (4.3) identifies the domain bounded by the two lines intersecting at point $(B/\varphi, -\theta'(s)B/\varphi)$ and touching the τ -axis at $+B$ and $-B$ respectively (Fig. 4.1). In general, the elastic domain may evolve between the upper and lower bounds determined by the maximum and minimum values attained by $\theta'(s)$.

In particular, for varying s the yield surface takes two different shapes in the $\{\sigma, \tau\}$ plane according to the sign of $\varphi - M$. Fig. 4.2(a) illustrates the case $M < \varphi$, corresponding to a material where Coulomb's friction φ is greater than the maximum (initial) slope M of the opening function, while Fig. 4.2(b) illustrates the dual case $M > \varphi$. Here, parameters B and φ have been kept at the same values of Fig. 4.2(a) and only M has been changed. Provided $\theta'(s)$ attains all the values in the interval $(-M, M)$ as s is varied, all admissible stress states lie in grey region represented in Figs. 4.2. In particular, the dark-grey region in the same figure, referred to as the *always-elastic domain*, corresponds to locally stable elastic stress configurations, i.e. every infinitesimal transformation from those states will remain elastic (in the sense that they do not imply any modification of s).

An interesting property, enjoyed by a wide class of crack profiles, is that $\theta'(s)$ is *discontinuous* and attains its *extreme* values in a neighborhood of the discontinuity points. More in detail, suppose that the even, null-average and p -periodic function $\omega(\xi/a)$, representative of the crack profile, can be expanded in converging Fourier's series of cosines

$$\omega\left(\frac{\xi}{a}\right) = \sum_n -\frac{A_n}{2} \cos\left(\frac{2n\pi\xi}{ap}\right), \quad (4.4)$$

with *all* the coefficients A_n of the same sign (without losing generality, suppose that $A_n > 0, \forall n$). Using (2.4), it can be shown that the corresponding opening function $\theta(\xi/a) = \theta(s)$ and its derivative may as well be expanded in Fourier's series in the form

$$\theta(s) = \sum_n A_n |\sin(n\pi s/p)|, \quad \theta'(s) = \sum_n (n\pi A_n/p) \operatorname{sgn}(\sin(n\pi s/p)) \cos(n\pi s/p), \quad (4.5)$$

respectively. Thus, from the assumed positiveness of all the coefficients A_n , it is clear that $\theta'(s)$ is discontinuous at $s = kp$, $k \in \mathbb{Z}$, and attains its *extreme* values in a neighborhood of such discontinuity points, i.e. at $s = kp^+$ and $s = kp^-$, where all the terms of the series (4.5) reach their corresponding extreme values. In particular, $\theta'(kp^+) = -\theta'(kp^-)$ and, consequently,

$$\theta'(s) \in (-M, M) \quad \forall s, \quad \text{where } M = \theta'(kp^+) = -\theta'(kp^-) > 0. \quad (4.6)$$

In the following, it will be supposed that crack profile $\omega(\xi/a)$ enjoys these properties.

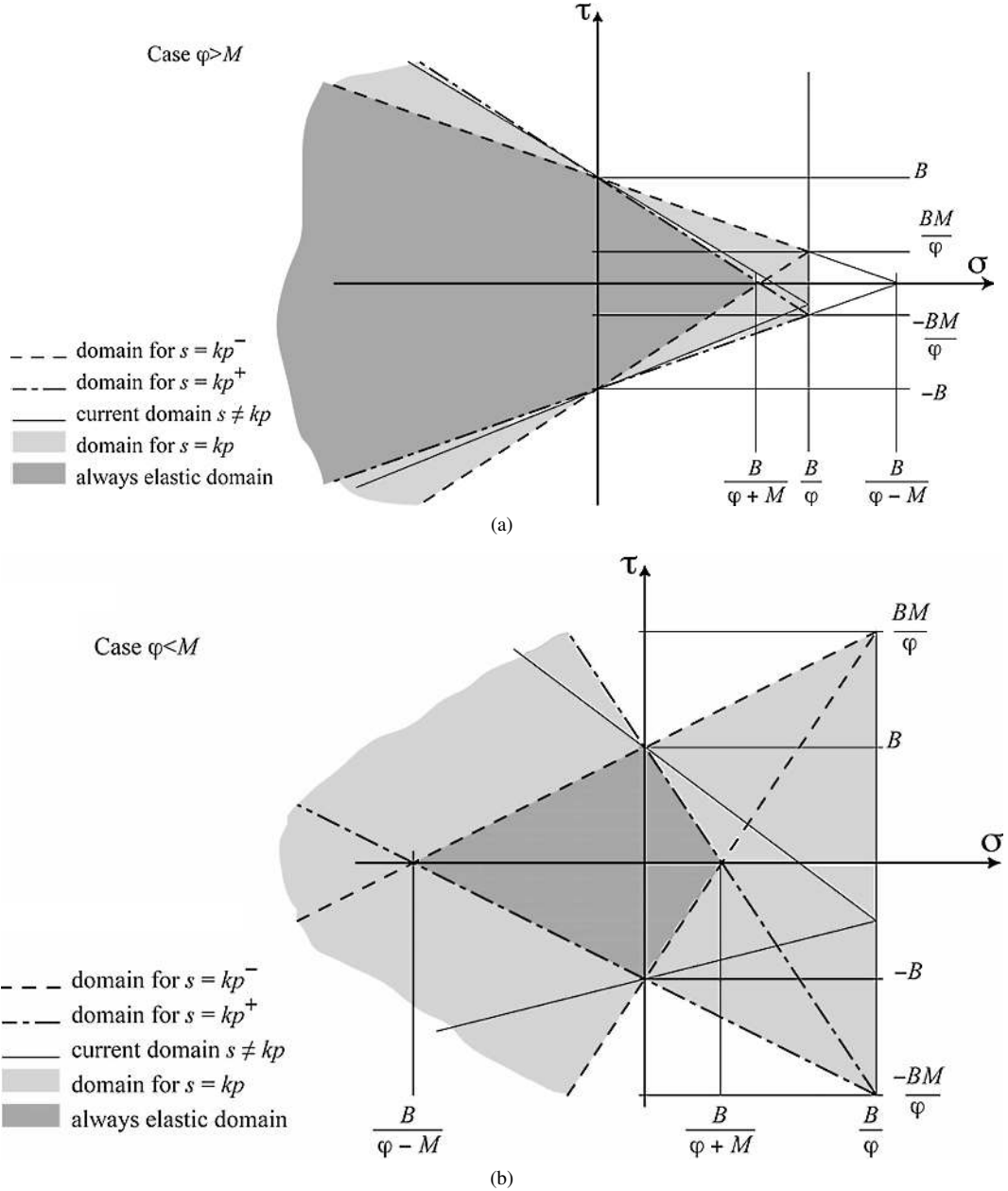


Fig. 4.2. (a) Elastic domains in the case $M < \varphi$. (b) Elastic domains in the case $M > \varphi$.

Indeed, the model calls for an interpretation of the discontinuity of $\theta'(s)$ at $s = kp$. If such a discontinuity was a sharp step, for any infinitesimal variation of s starting from $s = kp$ the yield surface would suddenly jump between two distinct configurations, represented by wedges whose vertexes are either at $(B/\varphi, -MB/\varphi)$ or at $(B/\varphi, +MB/\varphi)$ (see Fig. 4.1). However, such a material instability is not realistic. Instead, the discontinuity should be interpreted as the borderline case of a sequence of continuous functions, so that $\theta'(s)$ attains all the values of the interval $(-M, M)$ in a neighborhood of $s = kp$. In concise form, one may suppose that

$$-M \leq \theta'(kp) \leq M. \quad (4.7)$$

This position reflects the spirit of classical Coulomb's friction theory. Comparing (4.7) and (4.3) with $B = 0$, one finds that at $s = kp$ the admissible shear stress can be whatever but (in absolute value) less than a certain fraction of the compression stress.

In other words, all possible admissible states in the stress space, spanned while $\theta'(s) \in [-M, M]$, can be attained by a virgin body with no slip ($s = 0$). Of course, a crack shift of an integer multiple of its wave length cannot be distinguished by the state $s = 0$ and, consequently, in general the deductions for $s = 0$ are also true for $s = kp$.

Notice as well that an important consequence of (4.7) is that *stable yielding from the undistorted configuration* ($s = kp$) *cannot be produced by stress-driven paths*. In fact, at whatever small variation of s in a neighborhood of $s = kp$ would produce a jump of the fork towards the boundary of the admissible domain, where $\theta'(kp^\pm) = \pm M$. In this configuration the stress cannot be further augmented and s can be moved away from the zero value only by strain-driven deformations. On the contrary, starting from a configuration $s \neq kp$ where $\theta'(s)$ is locally invertible, a moderate stress variation may gently “push” the fork of Figs. 4.2, similarly to kinematic hardening in classical theory of plasticity.

Being bounded by straight lines, the current yield surface is obviously smooth except at the apex $\{\sigma, \tau\} = \{B/\varphi, -B\theta'(s)/\varphi\}$. This corner, as well as all the corners of the allowable domain (dark and light grey arrays in Figs. 4.2), do not entail any difficulty in computation. In fact, there is only one degree of freedom in the fork evolution, and no ambiguity is present when the representative point of the state of stress in the RVE coincides with the apex.

The two cases illustrated in Figs. 4.2(a) and 4.2(b) have an interesting physical interpretation. The case $M < \varphi$ of Fig. 4.2(a), characterized by a friction coefficient φ greater than the maximum slope M of the opening function $\theta(s)$, may be thought of as corresponding to a damaged material with “blunt teeth” crack profiles. In particular, the borderline case $M = 0$ corresponds to plane cracks and, for this shape, all the elastic domains coincide; sliding occurs at constant shear, and Mohr–Coulomb’s classical model, commonly used for soils, is recovered. The significance of the alternative condition $M > \varphi$, represented in Fig. 4.2(b), is that the effect of the opening function overcomes friction, as for cracks with “sharp teeth”. The borderline situation $M \rightarrow \infty$, when the opening function $\theta(s)$ has infinite slope at $s = kp$, is met by any crack profile that presents infinite slope at the nodal points.³ Now, the admissible-domain coincides with the half plane $\sigma < B/\varphi$, deprived of the two half-lines ($\sigma = 0, \tau < -M$) and ($\sigma = 0, \tau > +M$). An intermediate situation is $M = \varphi$, which leads to rectangular-shaped domains that can be easily deduced from Figs. 4.2(a) or 4.2(b).

It should also be remarked that when $M < \varphi$ the material response in uniaxial compression (with $\tau = 0$) is always elastic (Fig. 4.2(a)), whereas when $M > \varphi$ this is not true in general. In fact, the “kite-like” shape of the always-elastic-domain, etched in dark grey in Fig. 4.2(b), evidences that there exist configurations for which the elastic region may be modified by increasing the compression while maintaining fixed the shear stress. In both cases, the model predicts that indefinitely high compression can be withstood by virgin materials ($s = 0$) or materials where cracks have been relatively shifted of a multiple of the wavelength ($s = kp, k \in \mathbb{Z}$). The particular case $s = kp/2, k \in \mathbb{Z}$, corresponding to the contact of the crack lips at the summits of their wave-function profile, should be considered as a meta-stable equilibrium since any infinitesimal variation of s produces the crack closure under compression.

4.2. Response to cyclic actions

In order to illustrate some of the possible responses interpreted by the model, an ideal cyclic test is conceived of where the normal stress is maintained fixed at $\sigma = \sigma_0$, while the average shear strain γ is augmented starting from $\gamma = 0$ and then cyclically varied between the limits $-\gamma_0 \leq \gamma \leq \gamma_0$. Assuming that the strain in a RVE is homogeneous and the crack slip uniform, the state of stress is also homogeneous and defined by $\sigma = \sigma_0 \mathbf{e}_1 \otimes \mathbf{e}_1 + \tau (\mathbf{e}_1 \otimes \mathbf{e}_2 + \mathbf{e}_2 \otimes \mathbf{e}_1)$ and, from (3.3),

$$\gamma = \frac{\tau}{\mu} + s. \quad (4.8)$$

For fixed s and σ_0 , the yield conditions defined by (4.3) read

$$\begin{aligned} \tau &= (B - \sigma_0 \varphi) - \sigma_0 \theta'(s), & \text{case (A),} \\ \tau &= -(B - \sigma_0 \varphi) - \sigma_0 \theta'(s), & \text{case (B).} \end{aligned} \quad (4.9)$$

Consideration of the dissipation equation (4.2) and the expression (4.1) for S , lead to retain case (A) if \dot{s} is positive and case (B) if it is negative. Such conditions define all the yielding paths.

To systematically analyze the results of the model, it is convenient to distinguish whether the material is in tension or compression. For the sake of simplicity, only the case when ω is a saw-tooth function will be considered. For this crack shape, recall from (2.5) that the separation function $\theta(s)$ is the triangle function $A \text{Tr}(2s/p)$ and its derivative is piecewise constant, i.e. $\theta'(s) = \pm 2A/p = \pm M$, with jumps at $s = kp, k \in \mathbb{Z}$.

³ This case is particularly interesting for concrete. When cracking occurs along the aggregate contours, the crack profile is approximately piecewise semicircular (Walraven and Reinhardt, 1981). In this particular class of saw-tooth crack-profiles, the borderline condition $M \rightarrow \infty$ corresponds to a square wave function of the type $\omega(x) = aQ(2x/p)$, which offers a connection similar to a “Lego” brick game. Here, $Q(\cdot)$ is the periodic extension of the function $Q_1(\cdot)$, defined in the interval $[0, 2]$ as $Q_1(t) = 0$ for $t \in [0, 1)$ and $Q_1(t) = 1$ for $t \in [1, 2]$.

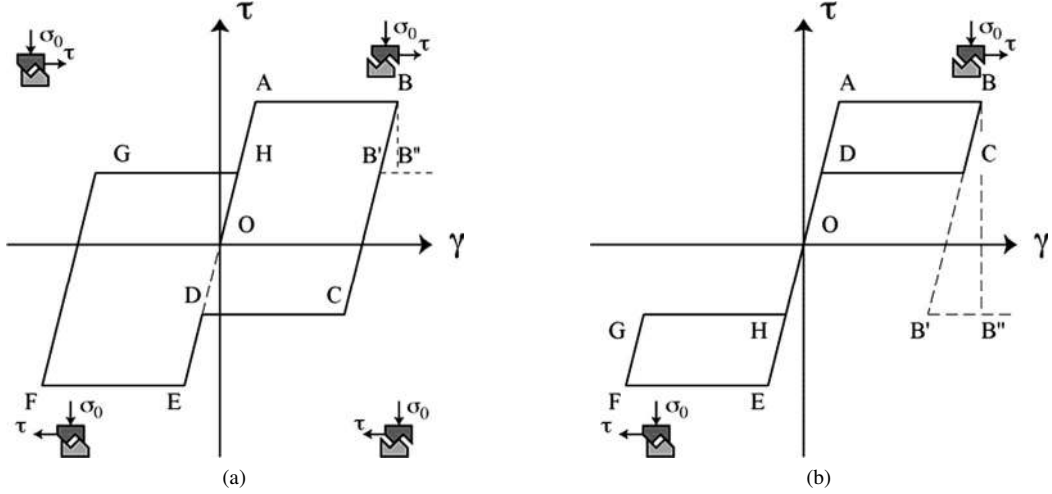


Fig. 4.3. (a) Hysteresis loop in the (γ, τ) plane for compressed specimens with saw-tooth cracks. (b) The pseudo-elastic response for reversible sliding (high compression and low friction).

4.2.1. Hysteresis loop in compression ($\sigma_0 < 0$)

When the average crack plane is compressed, the representative point of shear stress and strain in the RVE will follow the path $O-A-B-C-D-E-F-G-H-A \dots$ in the (γ, τ) plane of Fig. 4.3(a). The material starts to yield at point A for $\tau_A = B - \sigma_0(\varphi + M)$ and, afterwards, it follows a pseudo-plastic plateau. During unloading, starting at point B, a path parallel to the initial elastic branch is followed until the material yields again at C under the shear $\tau_C = -B + \sigma_0(\varphi - M)$. The distance from the γ -axis of AB is larger than the distance of the reverse yielding path CD because in the first case, due to the slope of the crack teeth, the compression load acts against yielding, while the contrary is true for path CD (compare the schematic representation of the crack profile and opening in Fig. 4.3(a)). At D, which is collinear with O and A, the crack has been closed ($s = 0$), and now the material can again regain stiffness. The material yields again at point E, whose abscissa τ equals a value opposite to that of point A. Discussion for points G and H is similar.

An interesting case is when the level of stress at D is greater than zero, so that the hysteresis loop is as depicted in Fig. 4.3(b). This case is attained when

$$-B + \sigma_0(\varphi - M) > 0. \quad (4.10)$$

But, recalling that σ_0 is negative, this condition can only be fulfilled when $M > \varphi$ for $\sigma_0 < -B/(M - \varphi)$, that is, for high compression combined with either low friction or sharp crack teeth, so that the yielding domains are of the type represented in Fig. 4.2b. Notice that in this (σ, τ) representation, all points representative of the stress history lie on a vertical segment on the left-hand side of the abscissa $B/(\varphi - M)$ because of (4.10), so that the shear level causing the elastic fork to move under reverse loading (point C in Fig. 4.3(b)) is greater than zero. Recall that, while sliding, there is competition between the driving shear stress τ and the effect of the compressive load. When φ is small when compared to the crack-tooth slope as in the case at hand ($\varphi < M$) reversible sliding may result, i.e., for high compression the crack closes by itself without the action of a shear force τ . This is why on the equilibrium paths CD and GH the shearing stress τ acts in a direction opposite to that of crack sliding, giving rise to a pseudo-elastic response.

When the sliding s exceeds the value $p/2$, i.e. for $\gamma > \tau_A/\mu + p/2$, the teeth of the crack lips have overcome the point when their vertices are in contact, so that now the compressive stress tends to move the crack profiles towards a configuration shifted of one tooth-length with respect to the original one. For what this response is concerned, the material acts similarly to the case $s < 0$, but an instability is now involved. To illustrate, suppose that in Figs. 4.3(a) or 4.3(b) point B corresponds to $s = p/2$. If the test was performed with a closed loop testing machine by controlling the crack slip s , the representative point would follow the equilibrium path $B-B'$, parallel to $H-A$ of the re-loading path. But if the test is strain-driven, point B would directly jump to point B'' , thus exhibiting a material instability. In conclusion, increasing γ the representative points would follow the path indicated with $O-A-B-B''$ in Figs. 4.3(a) and 4.3(b). The cases $s = p/2 + kp$, $k \in \mathbb{Z}$, may be discussed in exactly the same manner.

4.2.2. Hysteresis loop in tension ($\sigma_0 > 0$)

From a practical point of view this load condition is probably less interesting than the previous one, but it is worth being discussed because intriguing instability phenomena may occur in tensile specimens. Recall that one of the main hypotheses of

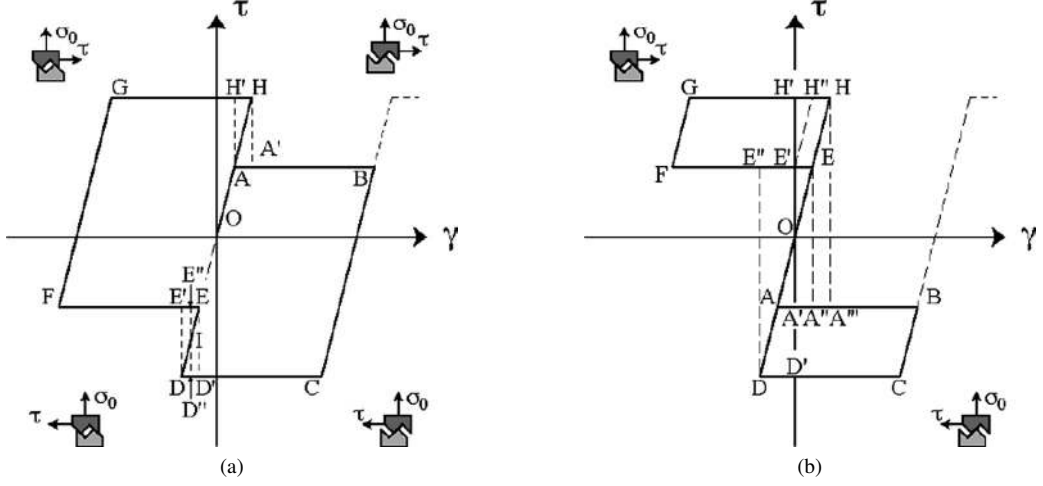


Fig. 4.4. (a) Hysteresis loop in the (γ, τ) plane for tensile specimens with saw-tooth cracks. (b) Pseudoelastic response for very high tensile load.

the model is that cohesive forces prevent complete material separation under moderate tensile loads, so that crack lips always remain in contact at some points during sliding. Comparing Fig. 2.3 and the discussion following (3.5), it is clear that a tensile load acts in favor of crack glide (“dilation-induced-shear”).

To illustrate the various possibilities, it is convenient to treat separately the situations (i) $0 < \sigma_0 < B/(\varphi + M)$ and (ii) $B/(\varphi + M) < \sigma_0 < B/\varphi$. The necessity of such a distinction is clear from the representation in the (σ, τ) plane of Figs. 4.2: here the stress path is represented by a vertical segment that intersects the always-elastic domain in case (i), but it does not in case (ii). At a qualitative level, the response is substantially the same for both the cases to which Figs. 4.2(a) and 4.2(b) refer to.

Case (i): $0 < \sigma_0 < B/(\varphi + M)$.

The corresponding (γ, τ) graph is represented in Fig. 4.4(a). The material starts to yield at point A at $\tau_A = B - \sigma_0(\varphi + M)$, with $\tau_A > 0$ because of the bounds on σ_0 , and reverse yielding occurs at point C for $\tau_C = -B + \sigma_0(\varphi - M)$, with $\tau_C < 0$ since the admissibility condition for (4.3) gives as well $\sigma_0 < B/\varphi$. What should be noticed is that tensile load favors sliding on path AB but acts against sliding on path CD, so that $|\tau_A| < |\tau_C|$. This explains as well why path AB is lower than GH and CD is lower than EF.

The loop $O-A-B-C-D-E-F-G-H-A$ in Fig. 4.4(a) is made of equilibrium paths, obtainable with a closed loop testing machine while controlling the crack slip in the specimen. On the base of the control signal, the machine should reverse the stroke movement at branch DE during path CDEF and the same at branch HA for path GHAB. If, on the other hand, the test is strain-driven, at D the point (γ, τ) representative of stress and strain in the specimen, would jump on branch EF at E'. From a physical point of view, notice that on DC the tensile load acts against shearing, but at D the crack closes and immediately afterwards the tensile loads favors shearing. Consequently, the material will exhibit a snap-through-like instability. Similar considerations show that there is a jump from H to A' during the re-loading path.

It might be questioned if, for example, the jump should occur at a point different from D on the segment DD'. Referring to Fig. 4.4(a), let us suppose that the jump is from D'' to E'' and let I represents the point of intersection between the lines D''E'' and OD. Recalling (3.9), it can be demonstrated that the driving force S is the same on both paths DD' and EE' and equals $-B + \sigma_0\varphi$. Since τ is constant on D'D'' and E'E'', we deduce from (4.8) that $\dot{s} \equiv \dot{\gamma}$ on both these paths. Consequently, denoting with Δs the length of the segment DD' (or EE'), the work dissipated on D'D'' + E'E'' is equal to $(B - \sigma_0\varphi)\Delta s$, whatever the position of D'' inside the interval DD'. Concerning the energy D^J dissipated in the jump D'' → E'', noticing from (4.8) that when γ is constant $ds \equiv -d\tau/\mu$ and that $s = 0$ at point I, recalling that $\tau = \mu\gamma$ on the line DA, one obtains

$$\begin{aligned}
 D_{D'' \rightarrow E''}^J &= \int_{D''}^{E''} (\sigma_0\theta'(s) + \tau) ds = \int_{D''}^I \frac{-(\sigma_0 M + \tau)}{\mu} d\tau + \int_I^{E''} \frac{-(\sigma_0 M + \tau)}{\mu} d\tau \\
 &= -\frac{2\sigma_0 M}{\mu} \tau_I + \frac{(\tau_{D''} + \tau_{E''})(2\sigma_0 M + \tau_{D''} - \tau_{E''})}{2\mu} = -\frac{2\sigma_0 M}{\mu} \tau_I + \text{const} > 0,
 \end{aligned} \tag{4.11}$$

where τ_I , $\tau_{D''}$ and $\tau_{E''}$ denote the shear stress at points I, D'' and E'' respectively. In conclusion, the highest dissipation is obtained when jumping from D to E', while the lowest dissipation is from D' to E (Fig. 4.4(a)). With analogous calculations,

the highest (lowest) dissipation is when the jump is from H (H') to A' (A). The fact that materials tend to dissipate as much energy as possible, corroborates the initial assertion that the path followed in a strain driven test would be $O-A-B-C-D-E'-F-G-H-A'-B$.

It should as well be mentioned that during the first loading branch OA , there is an equilibrium bifurcation right at point A , since both paths AH and AB are attainable. No dissipation is done along AH since $\dot{s} = 0$, whereas the power expended following the branch AA' , recalling (4.2), equals $(\sigma_0 M + \tau_A)\dot{s} \equiv (\sigma_0 M + \tau_A)\dot{\gamma}$. Since materials usually follow the path associated with the greatest dissipation, branch AH should be considered a *locus* of meta-stable equilibrium states. In fact, a whatever small perturbation of s starting from $s = 0$ would be sufficient to move the fork in Figs. 4.2 towards a configuration where the vertex is at $(B/\varphi, -BM/\varphi)$, for which shear stress greater than τ_A are not attainable.

Notice as well that a jump from A to H' can never occur, because it would correspond to a negative dissipation. In fact, using an argument similar to (4.11) and recalling from (4.7) that $\tau_A = B - \sigma_0(\varphi + M)$ and $\tau_{H'} = B - \sigma_0(\varphi - M)$, we obtain

$$D_{A \rightarrow H'}^J = \int_A^{H'} (\sigma_0 \theta'(s) + \tau) ds = \int_A^{H'} \frac{-(-\sigma_0 M + \tau)}{\mu} d\tau = \frac{2\sigma_0 M}{\mu} [\sigma_0(M + \varphi) - B] = -\frac{2\sigma_0 M \tau_A}{\mu} < 0. \quad (4.12)$$

This is clear also from a physical point of view since, in order to jump from A to H' , the crack would have to slip in a direction opposite to that of the shear stress τ (Fig. 4.4(a)). In any case, point H' could be attained through the action of an external “operator”, picking up the crack lips against the action of τ . Of course the opposite jump, from H' to A , occurs during the hysteresis loop.

Case (ii): $B/(\varphi + M) < \sigma_0 < B/\varphi$.

An even more intriguing phenomenon of instability may occur in tensile specimens when σ_0 , while respecting the admissibility limit (3.6), i.e. $\sigma_0 < B/\varphi$, satisfies condition $\sigma_0 > B/(\varphi + M)$. The corresponding equilibrium paths in the (γ, τ) plane are represented in Fig. 4.4(b), where what should be noticed is that paths AB and EF change the sign of τ with respect to Fig. 4.4(a), i.e., when $s > 0$ ($s < 0$) equilibrium can exist only when $\tau < 0$ ($\tau > 0$). This is because the tensile load is so high that friction alone cannot arrest the sliding of the crack, so that the action of a shearing force acting in the opposite direction is necessary in order to reestablish equilibrium. This may be thought of as a confinement effect, since it is necessary to apply a load τ opposed to γ in order to keep the material integrity.

Notice in particular that the origin ($s = \gamma = \tau = 0$) does not correspond to a point of stable equilibrium. In fact, there exist other four points, i.e. H' , E' , A' , D' which are in equilibrium at $\gamma = 0$. Reasoning as in (4.11) and recalling that $\tau_{H'} = B - \sigma_0(\varphi - M)$, $\tau_{E'} = -B + \sigma_0(\varphi + M)$, $\tau_{A'} = B - \sigma_0(\varphi + M)$ and $\tau_{D'} = -B + \sigma_0(\varphi - M)$, the energy dissipated while jumping from the origin to those points reads

$$D_{O \rightarrow H'}^J = D_{O \rightarrow E'}^J = D_{O \rightarrow A'}^J = D_{O \rightarrow D'}^J = \frac{1}{2\mu} [-B + \sigma_0(\varphi + M)][B - \sigma_0(\varphi - M)] > 0. \quad (4.13)$$

In words, the same energy is dissipated when jumping to either H' , or E' , or A' , or D' . Due to symmetry, the equivalence of points E' and A' , as well as H' and D' , is not surprising. The equivalence between E' and H' is due to the opposite effect of σ_0 and τ : the slip s at H' is greater than at E' , but while σ_0 produces a positive dissipation, τ is responsible of a negative dissipation and the two contributions compensate one another. Indeed, the correlation between points E' and H' (or between A' and D') may be explained paraphrasing the behavior of soil. In fact, the difference between the confining effect of τ at points, say, E' and H' recalls the same difference between *active* and *passive* confining pressure for a soil. In fact, at E' the shear τ *restrains* the crack from sliding towards the configuration of point F , whereas at H' the shear τ *produces* sliding towards the configuration of point H . Clearly $\tau_{H'} > \tau_{E'}$ because at H' the frictional forces have to be overcome.

Point O is not stable because the effect of the tensile stress σ_0 is sufficient to provoke the sliding of the inclined crack teeth and, consequently, if no shearing stress τ was applied, the material would irremediably break. Said more substantially *à la* Liapunov, despite the branch DAOEH being stable with respect to infinitesimal perturbations in τ or γ , it is unstable in the internal variable s , since a whatever small perturbation of s in a neighborhood of $s = 0$, is sufficient to move the fork in Figs. 4.2 towards one of the configurations $\theta'(0^\pm) = \pm M$. We may then suppose that a suitable confining constraint is applied such to maintain $\gamma = 0$ and the question arises whether, in this conditions, the material would jump towards E' or H' (the discussion for points A' or D' is symmetrical). Paraphrasing again the conceptual distinction between active and passive soil pressure, observe that at E' it is the material that pushes the constraint (“active” pressure), whereas at H' it is the constraint that pushes the material (“passive” pressure). If the constraint is not an actuator, its reaction would be the lowest to withstand the material pressure, similarly to the way in which a retaining wall withstands the action of a soil. Thus, the system would naturally jump towards E' (or its symmetric A'). This behavior is also confirmed by observing that elastic energy at H' (or D') is greater than at E' (or A'): the system should naturally tend towards the configuration which, for the same dissipation, corresponds to the lowest energy level.

Suppose now that, after applying σ_0 , the material jumps to the configuration A' . Increasing γ , the path $A'-B$ is followed. Reversing γ , branches BC and CD are attained, but at point D a snap-through instability phenomenon analogous to that discussed in (4.11) occurs, so that the representative point of the material state directly jumps from D to branch EF at E'' (a similar-in-type instability occurs from H to A'''). Therefore, in a strain-driven cycle the material would follow the path $O-A'-B-C-D-E''-F-G-H-A'''-B$. On the other hand, suppose that at the beginning the material had jumped to the configuration E' . In the (σ, τ) graphs of Figs. 4.2, such configuration corresponds to the point $(\sigma_0, -B + \sigma_0(\varphi + M))$, i.e. it is on the lower edge of the upper fork with vertex at $(B/\varphi, BM/\varphi)$. If at E' the shear γ is augmented, in Figs. 4.2 the representative point of the stress state enters the elastic domain. Correspondingly, in Fig. 4.4(b) the representative point follows a linear path parallel to the line $A-O-E$, and eventually reaches the branch GH at H'' . If γ is further augmented, the RVE configurations proceed towards point H on the branch $H''H$, finally jumping on A''' . In conclusion, the path followed by the representative point on Fig. 4.4(b) would be $O-E'-H''-H-A'''-B-C-D-E''-F-G-H-A'''-B$. Again, this behavior is pseudo-elastic in kind, but characterized by complex instability phenomena.

Whether the materials jumps from the origin to E' or A' depends upon the nature of the fluctuations in s , and may be considered a chaotic phenomenon, in the sense that whatever small variations in s around $s = 0$ may drive the material towards either E' or A' .

The case where s exceeds $p/2$, is represented in dashed lines on Fig. 4.4. In general, it leads to pure elastic paths at $s = kp$, $k \in \mathbb{Z}$.

5. Comparison with experiments and conclusions

The cases discussed in this paper are only a first attempt to illustrate some basic features of the proposed theory, whose potential is yet to be fully exploited. In our opinion, the strength of the approach consists in the description of what appears to be the crucial property to interpret the shear response of quasi-brittle materials: the *shear-induced dilatation*. This phenomenon is essentially due to the congenital roughness of developing cracks, naturally introducing a material intrinsic length-scale. For example in concrete, provided that cracking occurs through the cement matrix along the circumference of the aggregates, such a material parameter is of the same order of the aggregate average-diameter. When instead the aggregates are broken by developing fractures (as in high-performance concrete), crack roughness is determined by intrinsic irregularities whose size now defines the intrinsic length scale. The model here presented proposes a mesoscopic interpretation of the complex interactions between fracture surfaces through the definition of a “*equivalent crack-roughness*”, whose shape interprets and determines the shear-induced-dilatation phenomenon. Characteristic length scales for this theory are the crack profile amplitude and wavelength and the crack spacing (see Fig. 2.3).

There is a wealth of experimental evidence of the shear-induced-dilatation in quasi-brittle solids and traditional testing methods may provide an indirect assessment of the equivalent-crack-roughness. For example, Figs. 5.1(a) and 5.1(b) represent the apparatus used by Walraven and Reinhardt (1981) for testing concrete under shear loading. By loading the specimens as in Fig. 5.1(a), shear without moment is produced in the crack plane. Crack sliding induces the specimen dilatation that is

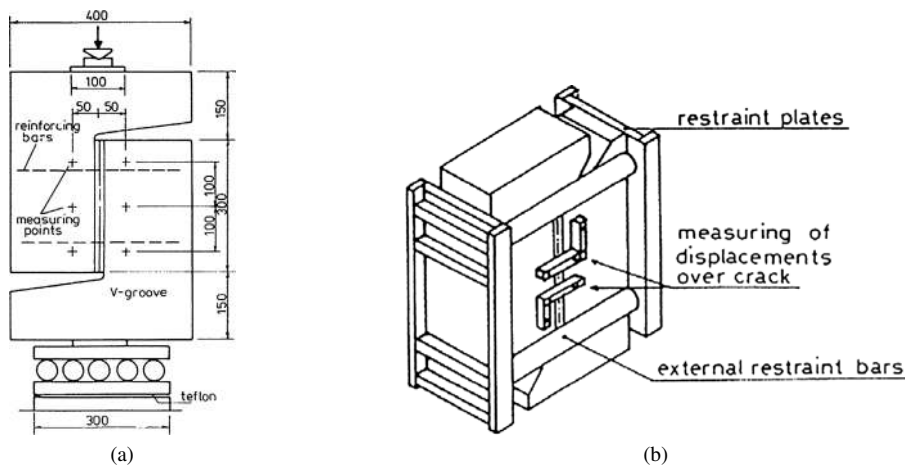


Fig. 5.1. (a) Geometry of the test specimens proposed by Walraven and Reinhardt (1981) to assess the shear response of cracked concrete. (b) Measuring gages and arrangement of restraint bars and plates on the specimen.

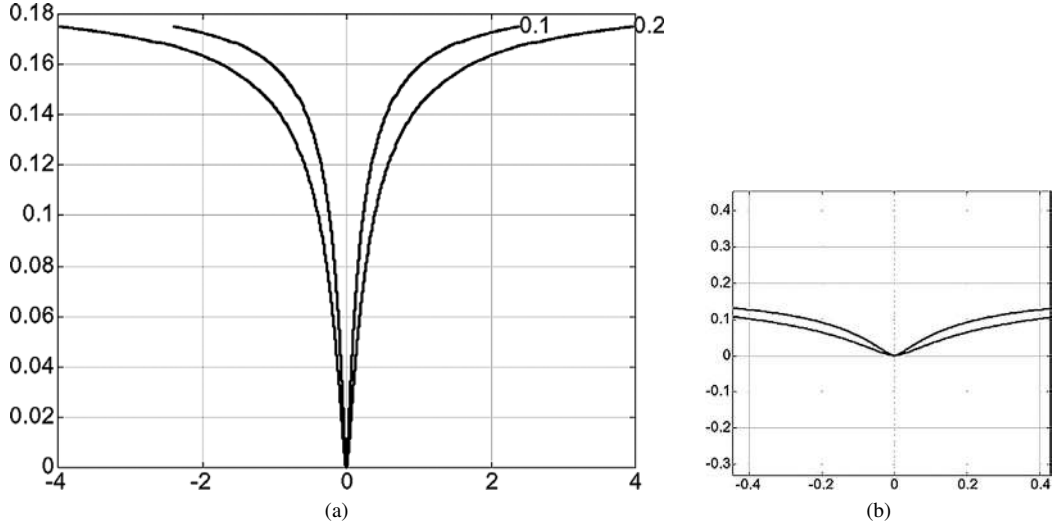


Fig. 5.2. Separation function $\theta = \theta(s)$ obtained from (5.2) for $f_{cc} = 59.1 \text{ N/mm}^2$, $\delta = 10 \text{ mm}$ and compressive stress either $\sigma = 0.2f_{cc}$ or $\sigma = 0.1f_{cc}$. (a) Axes with different lengthscale. (b) Magnification in a neighborhood of the origin (axes with equal lengthscale).

prevented by the restraint bars depicted in Fig. 5.1(b), so that crack plane is compressed by a normal stress, directly estimated by measuring the elastic elongation of the restraint bars.

The relative displacement over the crack plane is measured by gages placed as in Fig. 5.1(b). Let us denote with Δ and w the tangential (shear) and normal (dilatation) components of such displacement. If δ denotes the thickness of the material layer amenable to cracking (comprised between the two massive L-shaped blocks of Fig. 5.1(b)), the sliding s and the separation θ , defined as *per* Section 2 (Fig. 2.3), may be estimated by $s = \Delta/\delta$, $\theta = w/\delta$. Experimentally, one finds a definite, albeit complicated, relationship among shear stress τ , normal compression stress σ , slip s and separation θ , from which the equivalent crack-roughness can be consequently calculated.

To illustrate, consider the following expressions, interpolating the results of some relevant tests on concrete by Walraven and Reinhardt (1981):

$$\tau = -\frac{f_{cc}}{30} + [1.8(\theta\delta)^{-0.80} + (0.234(\theta\delta)^{-0.707} - 0.2) \cdot f_{cc}]s\delta, \quad (5.1)$$

$$\sigma = -\frac{f_{cc}}{20} + [1.35(\theta\delta)^{-0.63} + (0.191(\theta\delta)^{-0.552} - 0.15) \cdot f_{cc}]s\delta. \quad (5.2)$$

Here, f_{cc} denotes the concrete cubic compression strength in N/mm^2 , σ (positive when compressive) and τ are expressed in N/mm^2 and δ is measured in mm. For fixed σ , one can easily determine from (5.2) the expression $\theta = \theta_\sigma(s)$, plotted in Figs. 5.2 at two different scales, which represents the separation function introduced in Section 2 to describe the shear induced dilatation. The equivalent crack-profile can be consequently calculated through (2.3). Of course, the graphs of Fig. 5.2 are not periodic since they should be associated with *moderate* sliding, prior to crack-teeth surmounting.

What should be noticed, however, is that the experiments indicate the dependence of the separation function upon the normal stress σ . From a physical point of view this is not surprising, since the crack profile is surely modified by the presence the normal stress σ because of Hertzian contact and/or material wearing off. There is no substantial problem in developing the present model by allowing the dependence of θ upon σ , i.e. $\theta = \theta(\sigma, s)$. In particular, if σ is kept constant during the load-history the analysis of the material response is identical to that of Section 4, of course provided that θ is varied accordingly to the assumed dependence upon σ . Figs. 5.2 show for example the separation function θ obtained from (5.2) by setting either $\sigma = 0.1f_{cc}$ or $\sigma = 0.2f_{cc}$. The similarity between the two curves is quite evident and, since Hertzian contact blunts the crack asperities, it is logical that the lower curve corresponds to the higher compression. Notice as well that, although the different length scale used for the axes in Fig. 5.2(a) might suggest the contrary, in a neighborhood of the origin both profiles are smooth as *per* Fig. 5.2(b), which represents a magnification of Fig. 5.2(a) with axes of equal length-scale. This corroborates our previous conclusions about the continuity of $\theta'(s)$ at $s = 0$, leading to (4.7).

A micromechanically-motivated analysis of the possible dependence of the separation function upon the normal stress will be considered in further work, but even without such a refinement the present theory can interpret a wide range of structural responses. In particular, the results of tests on panels under shear and confinement reveals significant similarities with the cases

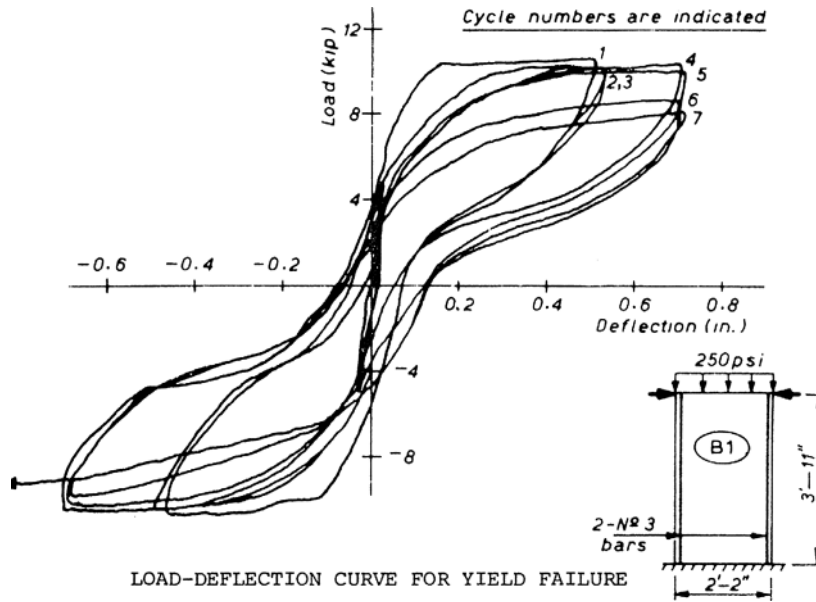


Fig. 5.3. Typical cyclic response of masonry walls under constant compression and variable shear (Mayes and Clough, 1975).

considered in Section 4. Fig. 5.3 shows for example the load-deflection curve for a reinforced masonry wall under constant compression and cyclic shear forces (Mayes and Clough, 1975). Of course, in this introductory paper only the simplest cases have been considered and the model here presented is nothing but minimal. Consequently the similarities between Fig. 5.3 and, say, Fig. 4.3(b), can only be considered at the qualitative level but, nevertheless, some interesting interpretations of the tests may be acquired from the model. For example, recalling the discussion for the case in Fig. 4.3(b), corresponding to condition (4.10), the theory seems to suggest that in the experiment of Fig. 5.3 displaced cracks can be closed by compression load without shear. Such a situation has been referred to as “reversible sliding” in Section 4.2.1.

Anyway, the present theory is versatile and amenable of substantial refinements. Not only could a closer representation of the experimental evidence be obtained by simply varying the crack profile, but it is also possible, with no substantial modification, to allow that the convex of elasticity varies its properties with increasing sliding. In fact, since frictional sliding wears out the crack profiles diminishing the shear resistance, future developments of our model will have to consider that the crack-opening mechanism may vary in time because of wearing out of crack-teeth. Such a deterioration phenomenon could be driven, as usually assumed in brake or clutch-disc design, by the frictional dissipated power $\int S \dot{s} dt$, already introduced in (4.2).

In conclusion, albeit tentatively, the simple theory here presented seems to be an appropriate tool to describe the response of cracked materials, in particular the shear-induced dilatation. Structured crack sliding appears to be the natural internal variable to describe the material state, with which a consistent thermodynamic force may be associated. In this way, the microscopic complexity of damage is interpreted at the mesoscopic level by only one function, representative of the crack profile. Just changing the shape of such a function allows a very wide spectrum of material responses to be consistently obtained. This theory could be combined with some recent analysis of the three-dimensional damage and may account for the fractal nature of the crack lips (Carpinteri, Chiaia and Cornetti, 2003; Amitrano and Schmittbuhl, 2002).

Acknowledgements

Partial support of the European Community under the Galileo program is gratefully acknowledged. The authors would also like to express their appreciation to Professor Ivo Iori (University of Parma, Italy) for helpful and stimulating discussion during the preparation of this work.

References

- Amitrano, D., Schmittbuhl, J., 2002. Fracture roughness and gouge distribution of a granite shear band. *J. Geophys. Res.* 107 (12), 1–16.
- Andrieux, S., Bamberger, Y., Marigo, J.J., 1986. Un modèle de matériau fissuré pour les bétons et les roches. *J. Theor. et Appl. Mech.* 5 (3), 471–515.

- Barenblatt, G.I., 1962. The mathematical theory of equilibrium cracks in brittle fracture. *Adv. Appl. Mech.* 7, 44–149.
- Bazant, Z., Planas, J., 1998. *Fracture and Size Effect in Concrete and Other Quasi-Brittle Materials*. CRC Press, New York.
- Belletti, B., Cerioni, R., Iori, I., 2001. Physical approach for reinforced-concrete (PARC) membrane elements. *J. Struct. Engrg. ASCE* 127 (12), 1412–1426.
- Benveniste, Y., Dvorak, G.J., Wung, E.C., 1989. On interacting cracks and complex configurations in linear elastic media. *Int. J. Solids Structures* 25, 1279–1293.
- Carpinteri, A., Chiaia, B., Cornetti, P., 2003. On the mechanics of quasi-brittle materials with a fractal microstructure. *Eng. Fract. Mech.* 70, 2321–2349.
- Del Piero, G., Owen, D., 1993. Structured deformations of continua. *Arch. Rational Mech. Anal.* 124, 99–155.
- Del Piero, G., Owen, D., 2000. Structured deformations. *Quad. Inst. Nazion. Alta Mat.* 58, Firenze
- Dyskin, A.V., Galybin, A.N., 2001. Solution for dilating shear cracks in elastic plane. *Int. J. Fract.* 109 (3), 325–344.
- Fond, C., Fléjou, J.L., Berthaud, Y., 1995. Interactions between cracks and circular holes in two-dimensional linear elastic media. *Eur. J. Mech. A Solids* 14, 73–96.
- Halm, D., Dragon, A., 1996. A model of anisotropic damage by mesocrack growth; unilateral effect. *Int. J. Damage Mech.* 5, 384–402.
- Halm, D., Dragon, A., 1998. An anisotropic model of damage and frictional sliding for brittle materials. *Eur. J. Mech. A Solids* 17 (3), 439–460.
- Halphen, B., Nguyen, Q.S., 1975. Sur les matériaux standards généralisés. *J. Mécanique* 14 (1), 38–63.
- Jefferson, A.D., 2003. Craft—a plastic-damage-contact model for concrete. I. Model theory and thermodynamics considerations. *Int. J. Solids Structures* 40 (22), 5973–5999.
- Kachanov, L.M., 1986. *Introduction to Continuum Damage Mechanics*. Kluwer, Dordrecht.
- Kaufmann, W., Marty, P., 1998. Structural concrete cracked membrane model. *J. Struct. Engrg. ASCE* 124 (12), 1467–1475.
- Lemaitre, J., 1992. *A Course on Damage Mechanics*. Springer-Verlag, Berlin.
- Lemaitre, J., Chaboche, J.L., 1984. *Mécanique des matériaux solides*. Dunod, Paris.
- Maji, A.K., Wang, J.L., 1992. Experimental study of fracture processes in rocks. *Rocks Mech. Rocks Engrg.* 25, 25–47.
- Mazars, J., 1986. A description of micro- and macroscale damage of concrete structures. *Engrg. Fract. Mech.* 25 (5), 729–737.
- Mayes, R.L., Clough, R.W., 1975. State-of-the-art in seismic shear strength of masonry – an evaluation and review. NSF report n. EERC 75-21, College of Engineering, University of California at Berkeley.
- Onat, T., 1984. Effective properties of elastic materials that contain penny shaped voids. *Int. Engrg. Sci.* 22 (8–10), 1013–1021.
- Pang, X.B., Hsu, T.T., 1996. Fixed angle softened truss model for reinforced concrete. *ACI Struct. J.* 93 (2), 197–207.
- Patton, F.D., 1996. Multiple modes of shear failure in rock. In: *Proc. 1st Cong. ISRM (Lisbon)*, vol. 1, pp. 509–513.
- Pensée, V., Kondo, D., 2001. Une analyse micromécanique 3D de l'endommagement par mésosfissuration. *C. R. Acad. Sci. Paris, Sér. II* 329, 271–276.
- Ragueneau, F., La Borderie, C., Mazars, J., 2000. Damage model for concrete-like materials coupling cracking and friction, contribution towards structural damping: first uniaxial applications. *Mech. Cohes.-Frict. Mater.* 5, 607–625.
- Schmittbuhl, J., Roux, S., Berthaud, Y., 1994. Development of roughness in crack propagation. *Europhys. Lett.* 28 (8), 585–590.
- Steigman, D.J., 1991. Analysis of a theory of elasticity for masonry solids. *J. Mech. Phys. Solids* 39, 534–553.
- Walraven, J.C., Reinhardt, H.W., 1981. Concrete mechanics, part A – theory and experiments on the mechanical behavior of cracks in plain and reinforced concrete subjected to shear loading. *Heron* 26 (1a), 1–68.